

This is the accepted manuscript made available via CHORUS, the article has been published as:

## Four-wave mixing microscopy with electronic contrast of individual carbon nanotubes

Tatyana Sheps, Jordan Brocious, Brad L. Corso, O. Tolga Gül, Desiré Whitmore, Göksel Durkaya, Eric O. Potma, and Philip G. Collins

Phys. Rev. B **86**, 235412 — Published 10 December 2012

DOI: [10.1103/PhysRevB.86.235412](https://doi.org/10.1103/PhysRevB.86.235412)

# **Four-Wave Mixing Microscopy with Electronic Contrast of Individual Carbon Nanotubes**

Tatyana Sheps<sup>1</sup>, Jordan Brocious<sup>1</sup>, Brad L. Corso<sup>1</sup>, O. Tolga Gül<sup>1</sup>, Desiré Whitmore<sup>2</sup>, Göksel Durkaya<sup>2</sup>, Eric O. Potma<sup>2</sup> and Philip G. Collins<sup>1\*</sup>

*1. Department of Physics and Astronomy, University of California at Irvine, Irvine, CA 92697 USA*

*2. Department of Chemistry, University of California at Irvine, Irvine, CA 92697 USA*

We review an extensive study of the factors that influence the intensity of coherent, nonlinear four wave mixing (FWM) in carbon nanotubes, with particular attention to the variability inherent to single-walled carbon nanotubes (SWNTs). Through a combination of spatial imaging and spectroscopy applied to hundreds of individual SWNTs in optoelectronic devices, the FWM response is shown to vary systematically with free carrier concentration. This dependence is manifested both in the intrinsic SWNT bandstructure and also by extrinsic and environmental effects. We demonstrate the sensitivity of the SWNT FWM signal by investigating SWNTs transferred from one substrate to another, before and after the introduction of chemical damage, and with chemical and electrostatic doping. The results demonstrate FWM as a sensitive technique for interrogating SWNT optoelectronic properties.

## **I. INTRODUCTION**

Carbon nanotubes (CNTs) display a rich set of optical and optoelectrical properties<sup>1-3</sup> that render them promising candidates for nanoscopic optoelectronic building blocks in circuits. This prospect motivates the need to develop sensitive tools for characterizing the optical properties of CNT devices. Since CNT fabrication methods generally produce heterogeneous mixtures of nanotubes, correlating the optical response to the electronic structure of CNTs is best carried out at the single nanotube level. In this regard, the sensitivity of optical microscopy techniques, employing either near-field or far-field detection, has proven sufficient for detailed examinations of the optical properties of individual nanotubes.<sup>4</sup>

Whereas the linear optical properties of CNTs have been the topic of numerous studies, the nonlinear optical properties of nanotubes have received comparatively little attention. CNTs are known to exhibit high third-order nonlinear susceptibilities,<sup>5,6</sup> a property that has propelled their use as saturable absorbers in laser cavities.<sup>7,8</sup> The high optical nonlinearity also enables nonlinear spectroscopic investigations, which offer a closer look at the ultrafast carrier dynamics in nanotubes. Nonlinear optical measurements, and four-wave mixing (FWM) experiments in particular, can be optimized to reveal detailed information on the ultrafast evolution of optical excitations; information that remains hidden in linear spectroscopic measurements. The sensitivity of FWM techniques to both electronic and vibrational excitations makes them attractive probes for dissecting the nonlinear optical response of CNTs. Photon echo<sup>9</sup> and coherent Raman FWM<sup>10</sup> experiments, for instance, have enabled direct recordings of electronic and phonon dephasing, which hold important clues toward the extent of exciton-exciton and exciton-phonon interactions in CNTs.

We have recently shown that the FWM technique can be extended to the level of individual nanotubes.<sup>11</sup> By making use of a dual-color picosecond excitation scheme, we collected coherent anti-Stokes Raman scattering (CARS) signals from both metallic and semi-conducting single-walled carbon nanotubes (SWNTs) on quartz substrates. In these FWM microscopy experiments, the detected signal was dominated by the electronic response of the nanotubes. Using femtosecond excitation, Myllyperkiö *et al.* demonstrated that a time-resolved version of the FWM scheme was capable of probing electronic dephasing of optical excitations in individual nanotubes.<sup>12</sup> In addition, a pump-probe version of FWM microscopy has been used to image SWNTs and characterize electronic relaxation in single nanotubes.<sup>13</sup> Furthermore, the FWM experiment can be optimized to record the vibrational response of individual SWNTs, as was recently shown by Furusawa *et al.* in tip-enhanced CARS experiments.<sup>14</sup> By resolving individual CNTs, these studies underline the utility of FWM microscopy and microspectroscopy for investigating their nonlinear optical properties.

FWM microscopy is capable of probing CNTs suspended on or adhered to surfaces, further enabling direct inspection of the optical response of CNT optoelectronic circuits. Because of the sensitivity of

CARS-type FWM to electronic structure and charge carrier dynamics, this nonlinear microscopy technique promises to be a suitable method for visualizing and characterizing CNTs under a variety of conditions. In this work, we systematically examine the sensitivity of the nonlinear FWM process to the electronic properties of SWNTs. In particular, we study the dependence of the FWM signal on various parameters including SWNT structural properties, SWNT conductivity, gating potential, and chemical oxidation state. Our results establish that the third-order nonlinear susceptibility as detected by coherent FWM microscopy is a useful probe for examining spatially dependent electrical and chemical changes in individual SWNTs.

## II. EXPERIMENTAL METHODS

CNT synthesis and device fabrication provided precise control over the quality and history of all the samples used for FWM experiments. Numerous recipes are available for CNT synthesis,<sup>15, 16</sup> and our implementation used a high temperature, chemical vapor deposition (CVD) technique tuned for high purity, wafer-scale SWNT devices. CNT growth was initiated through the use of catalyst particles derived from a water-soluble, ligand-terminated, icosahedral FeMo keggins molecule.<sup>17, 18</sup> The CVD substrates were 4" diameter wafers of either fused quartz or ST-cut single crystal quartz and of two thicknesses, 170 and 350  $\mu\text{m}$ . A 1000:1 dilution of a saturated solution of the keggins in ethanol was spun onto a wafer and allowed to dry in air. Oxidation in air at 700  $^{\circ}\text{C}$  collapsed the keggins into catalytically-active, solid particles suitable for growing dilute, isolated CNTs at a density of approximately 1  $\mu\text{m}^{-2}$ .<sup>17, 19</sup> The CVD process occurred in a custom, 115 mm quartz tube furnace operating at 940  $^{\circ}\text{C}$ . After an initial reduction of the particles in  $\text{H}_2$  (520 sccm) and Ar (3000 sccm), the addition of  $\text{CH}_4$  (1000 sccm) initiated the spontaneous nucleation and growth of SWNTs.<sup>17, 19</sup> Process variables such as the choice of substrate, residual  $\text{H}_2\text{O}$  concentration, and duration and concentration of  $\text{CH}_4$  flow all contributed to the diameter distribution, and could be tuned to grow double-walled and multi-walled nanotubes (MWNTs). Throughout this report, the acronym CNT is used deliberately to refer

to all types of carbon nanotubes, and the use of SWNT or MWNT is restricted to measurements on that particular variety. Purposeful distinction is necessary because of the very different optical and electronic properties of SWNTs and MWNTs.

After CVD synthesis, Ti, Cr, or Ti/Pt electrodes were defined on top of the randomly grown SWNTs using wafer-scale optical lithography. An undercut bilayer resist (S1808 on top of LOR-A1, MicroChem) was used to promote liftoff with clean interfaces. The separation between source and drain electrodes was 2  $\mu\text{m}$  or larger. Electrostatic gating was accomplished using either aqueous electrolytes in direct contact with the CNT device or else with a metal plate supporting the backside of the wafer. In the electrolyte case, the native Ti oxide surface layer prevents disruptive currents from flowing between the liquid and the CNT contacts.

The optical measurements that are the focus of this report were performed using a custom-built inverted microscope system interfaced with a femtosecond lightsource consisting of a Ti:sapphire laser (MaiTai, Spectra-Physics) and a synchronously pumped optical parametric oscillator (Inspire, Spectra Physics). The laser system provided two laser beams, one fixed at 820 nm and the second tunable throughout the visible and near-infrared. Laser excitation was focused through a 60x water-immersed objective lens to a sub-micrometer spot that was raster scanned over isolated CNTs and CNT devices. Excitation and imaging were performed through the quartz substrate, in an epi configuration depicted in Figure 1(a). Signals were collected into a 400- $\mu\text{m}$  diameter multimode optical fiber (Ocean Optics - P400-2-VIS-NIR) and directed to either a synchronized PMT (Hamamatsu R6357) to generate two-dimensional images, or a spectrometer (Semrock SP01-785RS-25 short pass edge filter, Andor SR303i spectrometer, and Andor DU401A-BV CCD) to spectrally resolve the optical signal. Typical pixel dwell times of 40-60  $\mu\text{s}$  allowed for rapid scanning, but acceptable signal-to-noise for weak FWM signals required the averaging of 60 to 200 individual measurements, resulting in effective pixel dwell times in the 2 – 12 ms range.

FWM images were acquired by exciting a CNT with a pair of pulsed excitations at pump ( $\omega_p$ ) and Stokes ( $\omega_s$ ) frequencies, and collecting emission at the anti-Stokes frequency  $\omega_{as} = 2\omega_p - \omega_s$ . In the non-interferometric detection configuration employed here, the FWM signal results from a parametric process in which the initial state and final state of the material are identical. One of the dominant coherent FWM pathways is depicted in the energy level diagram of Fig. 1(b), but other pathways may contribute to the signal as well.<sup>20</sup> Measurements were performed using one of two pairs of excitation wavelengths: 820 and 943 nm, 725 and 820 nm. Note that the excitations at  $\omega_p$  and  $\omega_s$  were generally not tuned to the conventional SWNT optical resonances  $E_{11}$  or  $E_{22}$ , and instead excited carriers into the small but nonzero density of states within the conduction band [Fig. 1(b)]. The signal at  $\omega_{as}$  was filtered using dichroic mirrors and emission filters (Chroma NC112708-765dcspxr, NC086771-680dcspxr, and NC207524-HQ650/40m-2p, and Semrock FF01-720/13-25BP depending on the excitation pulse pairs used). Unless noted otherwise, all measurements were collected at zero time delay between the pump and the Stokes pulses. When imaging individual CNTs, the excitation polarization was always aligned parallel to the CNT to maximize the FWM signal. All of the measurements were performed using 150 fs pulses at a 80 MHz repetition rate. Laser power was limited to 5 to 8 mW, which generated acceptable signal-to-noise levels without damaging individual CNTs.

Figs. 1(c) and 1(d) show a typical FWM image and intensity profile for a single SWNT. Away from the metal electrodes, the image contrast was entirely due to the SWNT nonlinear optical response and its intensity above the dark count rate of the detector. The quartz substrate was found to contribute almost no measurable signal at  $\omega_{as}$ . We define a FWM intensity by normalizing the observed signal to the background rate and then performing a line-by-line averaging of pixels parallel to the SWNT axis. The resulting average is plotted as a function of distance  $\Delta x$  away from the SWNT position, as shown in Fig. 1(d). Despite careful attention, an accurate quantitative comparison of FWM intensities from different CNTs was complicated by a sensitive dependence on excitation power, averaging time, PMT gain settings, laser alignment and focus, and the particular filters used in the acquisition path. As a result,

meaningful comparisons of FWM intensities are often restricted to measurements using identical acquisition settings. This requirement complicates many forms of direct comparison, since different experiments often required modified acquisition settings. For example, FWM imaging in liquid electrolytes required much higher excitation powers than imaging in air. In this report, individual figures only report multiple FWM intensities when the data were acquired simultaneously in a single image, or else could be normalized to each other in a reproducible and meaningful way. Relative intensities among different figures might not be quantitatively comparable.

In order to study FWM of CNTs, and in particular the factors that lead to variations in FWM intensity, hundreds of individual CNTs were imaged and also characterized by independent techniques. Sample variability was addressed by restricting investigation to CNTs that were relatively straight, uniform in diameter, and contaminant-free. To this end, every device was electrically characterized, imaged by noncontact atomic force microscopy (AFM), and further imaged by scanning electron microscopy (SEM, JEOL 6060 at 1 kV) before and after optical measurements. Where possible, Raman spectra were collected with a confocal microscope using one of three fixed excitations at 405, 532, or 785 nm (Renishaw inVia). Fabricating the devices with very dilute CNTs and alignment marks made it straightforward to repeatedly locate the same SWNT using each of the different techniques. For example, the inset to Fig. 1(c) shows an SEM image at the same location as the FWM image, and an additional AFM image was acquired of the same CNT. Electrode fabrication using Ti electrodes was particularly advantageous because, unlike the quartz substrate, Ti exhibits a strong FWM signal for the excitation conditions employed here. The Ti electrodes allowed us to rapidly scan large areas, repeatedly locate the same CNTs, and maintain optimum image focus. Unfortunately, at the gain and dwell time required for observing SWNTs, the much stronger Ti signal is usually saturated as shown in Fig. 1(c), making it unsuitable for use as a calibration from device to device.

### **III. RESULTS AND DISCUSSION**

The sensitivity of the FWM response to the material properties of the CNT gives rise to a significant variability of the nonlinear signals in nanotube samples, as CNTs vary widely in morphology from one sample to another. Even along the length of a single CNT, the FWM intensity can change drastically due to kinks, points of high strain and curvature, or contaminant particles independently identified by AFM. This report describes the FWM response of CNTs and each of the causes of variation in that response, with results organized into four sections. Section IIIA begins by describing the nature of the optical FWM signal, in particular identifying the spectrally-resolved, coherent component. Section IIIB describes the differences in the FWM response that are due to CNT structural effects like diameter and chirality, while Section IIIC focuses on extrinsic variation caused by environmental effects. The results conclude with section IIID discussing the electronic resonance contributions to the FWM signal.

### A. The FWM Signal

When illuminated by two laser pulses at  $\omega_p$  and  $\omega_s$ , numerous optical processes are possible in CNTs. This report is specifically concerned with coherent FWM as detected at the anti-Stokes frequency  $\omega_{as} = 2\omega_p - \omega_s$ . The parametric FWM process, as depicted in Fig. 1(b), probes  $\chi^{(3)}(-\omega_{as}; \omega_p, -\omega_s, \omega_p)$  and is expected to be electronically enhanced whenever  $\omega_p$  or  $\omega_{as}$  is close to a one-photon allowed optical transition in the material.<sup>20</sup> In addition, the FWM signal is strong whenever the material exhibits allowed resonances at  $(\omega_p - \omega_s)$  or, alternatively, at  $(\omega_p + \omega_s)$  (diagram not shown). Previous work on individual SWNTs has shown the feasibility of detecting the Raman mediated, vibrational contribution to the FWM signal.<sup>14</sup> In this work, we focus predominantly on the dependence of the electronic FWM components on various parameters and experimental conditions.

Experimentally, we limit signal acquisition to the coherent, spectrally-resolved emission at  $\omega_{as}$ . However, spectral filtering alone was insufficient to quantitatively isolate the FWM component, especially for weak signals from SWNTs. As described below, the desired FWM signal is accompanied by a spectrally broader, incoherent luminescence. Figure 2 provides an example of emission from a 10-



nm diameter MWNT. Using a time delay  $\Delta t$  between the two excitation pulses, we observed two different emission components at  $\omega_{\text{as}}$ . The component of interest, labeled FWM in Fig. 2(a), occurred within a  $\sim 200$  fs temporal window around zero time-delay. As the electronic dephasing times are faster than  $100$  fs<sup>12</sup>, the temporal width of the FWM signal is dictated here by the duration of the pulses rather than by ultrafast dynamics of the material. Beyond the ultrafast coherent FWM response, an additional two-photon excited luminescence (TPEL) was observed at longer time delays. The luminescence contribution, which spectrally overlaps with the FWM signal, persists even at zero time delay, which complicates a straightforward separation of the coherent and incoherent contributions to the signal.

The longer-lived luminescence was subsequently examined by spectrally resolving the emission using either single- or dual-color excitation. Fig. 2(b) depicts emission spectra acquired at  $\Delta t = 0$  in both cases. Whereas the  $\omega_p$  and the  $\omega_s$  beams both contributed weakly to the incoherent emission, the TPEL contribution stemming from the joint  $(\omega_p + \omega_s)$  excitation at  $\Delta t = 0$  was significant, as shown in Fig 2(b). The TPEL is spectrally broad and spans the 600 nm to 760 nm range of the spectrometer grating. In addition, at  $\Delta t = 0$ , the FWM signal appeared at  $\omega_{\text{as}}$  (which in this example was tuned to a wavelength of 725 nm) on top of the TPEL background. The inset to Fig. 2(b) shows similar, two-color measurements performed at  $\Delta t = 0$  and 1 ps, confirming that the FWM peak at  $\omega_{\text{as}}$  completely disappears while the incoherent background decreases yet remains visible.

The broad TPEL contribution is an asymmetric function of the time delay between the pump and Stokes pulses. The TPEL signal is significantly stronger when the pump precedes the Stokes pulse, and weaker when the Stokes precedes the pump pulse. Furthermore, the TPEL remains significant for positive time delays well over 1 ps, suggesting that the enhanced TPEL is the result of the excitation of a long-lived state by the pump followed by a Stokes-induced excitation to a state that is coupled to a luminescent transition. The observation of luminescence resulting from the excitation of two-photon accessible states in CNTs is interesting, as luminescence in the visible range of the spectrum is not commonly observed in pristine CNT systems. However, the details of the TPEL signal require

investigation that is beyond the scope of this work. Instead, we focus primarily on distinguishing the FWM signal from this TPEL background.

By varying  $\Delta t$  and switching between single- and dual-color excitation, the FWM and TPEL components were successfully identified, separated, and measured on many individual SWNTs and MWNTs. Figure 3 shows typical spectra at  $\Delta t = 0$  from three devices, where the TPEL and FWM components can be easily identified by eye. As shown in the figure, the TPEL component did not change dramatically from one sample to another, although it was generally strongest in metallic SWNTs and MWNTs. This trend contrasts sharply with single photon luminescence, which is usually quenched in metallic SWNTs or CNTs on substrates.<sup>21, 22</sup>

While the TPEL background is relatively small in Figs. 2 and 3, it can be the primary emission component when the FWM amplitude becomes very small. Furthermore, the FWM peak at  $\omega_{\text{as}}$  is narrow whereas the TPEL is spectrally broad. Thus, the successful acquisition of real space CNT FWM images depends critically on proper filter selection. The FWM images and results at  $\Delta t = 0$  described here were exclusively acquired using an emission filter with a narrow bandwidth of 13 nm centered near  $\lambda_{\text{as}}$ , except for a portion of Section D that investigates excitation resonances with a wider bandwidth. Under these conditions, some FWM intensity was sacrificed to keep the TPEL contribution at an absolute minimum, typically around 10% of the total signal. For comparison, the data taken using a transmission window of 43 nm at  $\Delta t = 0$ , resulted in an apparent FWM:TPEL ratio as low as 2:1. The improved fidelity of the narrow filter was critical for accurate measurement of very small FWM signals from SWNTs, and the variability of those signals that is described in the following sections.

## **B. Dependence on CNT Type**

As shown in Fig. 3, the intensity of the coherent FWM emission shows significant dependence on the particular CNT being imaged. First and foremost, this variation is driven by a strong dependence on CNT diameter, with larger CNTs having greater FWM signals.<sup>11</sup> As previously reported, the FWM intensity

from SWNTs with outer diameter  $D$  increases proportionally to  $D^2$ , because the coherent FWM signal scales quadratically with the number of free carriers  $N$ .<sup>23</sup> The functional form of the diameter dependence, then, is merely indicative that  $N$  is proportional to diameter or, more precisely, to the number of carbon atoms in the focal area. This simple rule can be extrapolated to the more complex case of MWNTs, which have many internal shells. For MWNTs,  $N$  is approximately quadratic in  $D$ , leading to a more sensitive  $D^4$  dependence of the FWM intensity in these larger CNTs.<sup>11</sup> The very rapid increase of FWM intensity with  $D$  means that MWNTs are bright and straightforward to resolve, even under non-optimum FWM imaging conditions. SWNT signal intensity, on the other hand, is often close to the quantum-limited noise of the detector.

Compared to diameter, the length of a particular CNT appears to have no effect on the FWM intensity. Long and short CNTs can have the same FWM intensity, as long as the nanotube is longer than the width of the focal probing spot. To further test the length dependence, long individual SWNTs were severed with a high-powered laser beam. No appreciable difference was observed in the FWM intensity of an initial SWNT and its shortened segments. These observations prove that FWM is primarily a local probe on the sub-micrometer scale, insensitive to distant tube ends or defects.

After accounting for the dependence on diameter, the FWM intensity levels observed from SWNTs can be sub-divided into three categories. Electrical device characterization and resonant Raman measurements prove that the brightest FWM signals always come from metallic SWNTs (m-SWNTs). Semiconducting SWNTs (s-SWNTs), on the other hand, divide into two possible categories of dim and completely dark. Figure 4 provides examples of this categorization among four SWNTs imaged simultaneously. Fig. 4(a) is an SEM image locating four SWNTs, while Fig. 4(b) depicts their relative FWM intensities. Two m-SWNTs connected in parallel (upper left) are bright, while a s-SWNT connected to three different electrodes (lower center) is nearly invisible. The white arrow in the figure indicates the excitation polarization, here aligned parallel to the s-SWNT to generate the largest possible FWM signal from it. As described in previous work, the polarization dependence follows a  $\cos^6\theta$  dependence, confirming that the FWM signal scales to the third order with the incoming excitation

intensity.<sup>11</sup> Due to this polarization dependence, the m-SWNTs in the image appear only half as bright as it might. Therefore, the image underreports the contrast variation possible from one SWNT to another.

Fig. 4(c) summarizes the correlation between diameter, electronic structure, and FWM intensity for eleven SWNTs that were imaged under identical conditions. Each data point represents an ideal SWNT specimen with a well-resolved diameter, unambiguous electronic structure, and noise- and artifact-free FWM intensity. Approximately one-third are bright m-SWNTs falling along a curve of  $D^2$  as discussed above. Of the remaining two thirds that are s-SWNT, some suggest a second curve with approximately half the intensity of the m-SWNTs, but a large fraction of the s-SWNTs have no discernible FWM intensity above the background. The separation of s-SWNTs into two distinct categories can be explained by environmental doping effects, as discussed in the following section.

### **C. Sensitivity to CNT Environment**

The FWM imaging experiments were performed through a transparent quartz substrate while the CNT remained exposed to its environment. This configuration provided an opportunity to study the same CNT in different gas or liquid environments, and to apply electrostatic gates using an electrolyte. For example, neither Ar nor NH<sub>3</sub> gas environments had any noticeable effect on FWM intensity, although Ar and similar inert gases did help to limit oxidative damage in the CNT at the highest excitation power levels. In liquids, the FWM intensity decreased substantially, an effect attributed to the refractive index change at the SWNT-water interface.<sup>24</sup> Despite this signal decrease, electrochemical control over a liquid environment proved to be an effective and versatile way to change the FWM response. This section describes FWM variations that are attributed to electrostatic effects at small electrochemical potentials and covalent oxidation at higher electrochemical potentials. A third portion of this section describes the dependence of the FWM response from CNTs when changing the crystal properties of the quartz substrate.

#### **C.1. Noncovalent Electrostatic Gating**

Semiconducting SWNTs (s-SWNTs) are characterized by a diameter-dependent bandgap in the range of 0.5 – 1.9 eV.<sup>3, 25</sup> The Fermi level  $E_F$  of a s-SWNT can be electrostatically tuned into this bandgap, thereby depleting the device of carriers and turning off all conduction. This field-effect transistor response has been widely investigated using various geometries of metallic gate electrodes<sup>26, 27</sup> and liquid electrolytes,<sup>28, 29</sup> the latter of which are compatible with epi FWM measurements. In our implementation, Deionized (DI) H<sub>2</sub>O was confined under a cover slip and biased at a potential  $V_{\text{liq}}$  using a Pt counter electrode. Resolving gate modulation of the FWM signal required particular care: among all CNTs, s-SWNTs have the highest sensitivity to gating, but they also have relatively low FWM intensities, which is particularly low when the SWNT is immersed in an electrolyte solution. Therefore, we will limit our discussion to the brightest s-SWNTs, whose gate-induced variations in the FWM signal could be clearly resolved in liquid.

Figure 5(a) shows the variation in FWM intensity and conductance observed when gating a typical s-SWNT. Negative gating always accumulates carriers in these p-type SWNTs, while positive gating depletes them. Accordingly, a steep increase in conductance was observed for  $V_{\text{liq}} < 0$ . As shown in Fig. 5(a), the FWM signal tracked the conductance and was approximately proportional to it. The conductance signal could also be modulated using a back gate electrode at bias  $V_{\text{bg}}$ , though this gating occurred through the quartz and correspondingly had a much smaller capacitance. Fig. 5(a) directly compares the voltage scales for the liquid and back gate techniques. Fig. 5(b) shows the energy diagram and excitation scheme that correspond to the gating of a s-SWNT. In this figure,  $E_F$  is depicted below the valence band edge to illustrate the case  $V_{\text{liq}} < 0$ .

Even though it matches the SWNT conductance, the FWM response to gating is opposite to what is normally observed in conventional, single photon measurements of s-SWNTs. Single-photon resonant absorption and fluorescence occurs by pumping the primary optical transition  $E_{11}$ . Fluorescence at  $E_{11}$  is strong for every  $E_F$  position within the band gap, but then it bleaches when  $E_F$  is gated below the valence band edge, as this causes the van Hove singularity of the valence band to become unoccupied.<sup>21, 30</sup> The FWM response exhibits the exact opposite behavior, being undetectable for  $E_F$  values within the band gap

and growing stronger as  $E_F$  extends into the valence band. This energy dependence results from resonant FWM amplification by unoccupied states at the  $\omega_p - \omega_s$  transition. No unoccupied state exists at this transition when  $E_F$  is in the band gap, nor until  $E_F$  passes below the band edge by the amount  $\hbar(\omega_p - \omega_s)$ . As  $E_F$  is gated lower in energy, absorption at  $\omega_p$  and FWM remain significant, while single-photon fluorescence at  $E_{11}$  is substantially quenched. As a consequence, energy- and time-resolved FWM measurements at  $\omega_{as}$  can be performed with background-free, high sensitivity detection.

A final notable aspect of the curves in Fig. 5(a) is a downturn of the FWM intensity for  $V_{liq} < -0.1$  V. The 20% decrease in FWM intensity between  $V_{liq} = -0.1$  and  $-0.2$  V reflects the decreasing free carrier concentration (i.e. the density of states) that occurs as  $E_F$  extends further into the valence band. Similar peaking near the band edge has been measured experimentally in electrical capacitance<sup>31, 32</sup> and optical absorption measurements,<sup>33, 34</sup> and FWM data from other s-SWNTs supports this assignment. The conductance, on the other hand, plateaus to a level limited by contact resistance at the SWNT-metal electrode interface. Thus, the conductance plateau in Fig. 5(a) is not an intrinsic response of the SWNT, and it is independent of carrier concentration.

Fig. 5(c) shows comparable measurements on a m-SWNT. At room temperature, conductance modulation of 25 to 75% is typical for m-SWNTs as  $E_F$  is varied, indicative of small band gaps induced by strain or disorder.<sup>35</sup> Otherwise, m-SWNTs cannot be completely depleted or gated to zero conductance at any value of  $V_{liq}$ . As shown in Fig. 5(c), the FWM intensity and conductance of a m-SWNT shared similar gate sensitivities, varying in this device by approximately 50%. A corresponding energy diagram in Fig. 5(d) portrays the critical  $\omega_p - \omega_s$  transition and the availability of unoccupied states at every  $E_F$  value. It is noted that other parametric FWM pathways can also contribute to the signal. Nonetheless, the pathways sketched in Figures 5(b) and 5(d) are plausible contributions to the FWM signal that are in agreement with the gating experiments.

In both s-SWNTs and m-SWNTs, good agreement is observed in the gate modulation of FWM intensity and conductance. However, no similar correlations are observed between FWM intensity and

the maximum value of the conductance, the contact resistance, or the composition of the contact metal. All of these device aspects are understood to be extrinsic to the SWNT physics and therefore decoupled from the mechanisms which determine the FWM intensity. Nevertheless, one extrinsic device aspect has indeed proven critical to the interpretation of FWM imaging, and this is the gate voltage threshold  $V_T$  at which conductance reaches its minimum.  $V_T$  reflects the degree of chemical doping present in a particular SWNT. Variations in substrate chemistry, surface contamination, and Schottky barrier effects routinely cause  $V_T$  to vary by  $\Delta V_{liq} = 0.1 - 0.2$  V from device to device, and by as much as 0.4 V from one wafer to another.

This  $V_T$  variation is responsible for the range of FWM brightness observed in s-SWNTs and the FWM-dark categorization of some s-SWNTs in Fig. 4(c). The majority of our measurements were performed in air rather than with an electrolyte solution because in air the FWM intensity is higher, implying that less excitation power can be used. Unfortunately, measurements in air do not control  $E_F$ , leaving it to vary with local surface properties. Those SWNTs with  $V_T > 0$  will have free carriers without additional gating. The s-SWNT in Fig. 5(a) is an example of this type, where the FWM intensity is nonzero at  $V_{bg} = 0$  V. The alternate case occurs for SWNTs with  $V_T < 0$ , which are fully depleted at  $V_{bg} = 0$  V and are therefore FWM dark in air. Device-to-device variation in  $V_T$  was particularly obvious when many s-SWNTs were in the same field of view, because FWM imaging very clearly resolved some s-SWNTs but not others. This sensitivity to surface gating has negative implications for FWM as a general imaging technique, because it implies that either  $V_T$  must be tightly controlled or else the SWNTs must be intentionally doped. Doping all of the s-SWNTs to a conductive state, such as with the electrostatic technique depicted here, allowed the vast majority of s-SWNTs to be imaged. Less than 10% of all s-SWNTs remained dark under the conditions tested here.

## C.2. Covalent Electrochemical Modification

In the same configuration used for electrostatic gating, the electrochemical potential can be increased to the point that covalent addition reactions are promoted on a CNT sidewall. The effects of this

oxidation on SWNT conductivity have been studied in some detail,<sup>36-39</sup> and here we applied the same methods to FWM experiments. Oxidation reactions were driven in either 1 M HCl, 1M H<sub>2</sub>SO<sub>4</sub>, DI H<sub>2</sub>O, or 70% glycolic acid (GA), creating –Cl, –OH, or –COOH covalent adducts, respectively. While oxidation was sometimes performed on the FWM microscope *in situ*, more precise control was achieved by using a separate liquid cell optimized for monitoring CNT conductivity during oxidation reactions. Being electrochemically controlled, the oxidation could be halted at any stage in order to perform FWM measurements with increasing degrees of disorder. Separately, AFM and Raman imaging confirmed that CNTs maintained their apparent diameters and overall topography, indicating that the treatments did not induce substantial structural damage.

In general, oxidizing CNTs caused the FWM intensity to decrease, indicating that the signal is indeed sensitive to covalent sidewall attachments. SWNTs proved difficult to study because their low FWM intensity became undetectable after oxidation. In fact, FWM intensity disappeared in SWNTs well before disorder became evident in their Raman spectra. MWNT experiments proved to be more instructive because MWNTs' high FWM intensities allowed gradual decreases to be followed through multiple oxidation cycles. As an example, Figure 6(a) shows measurements performed on a 6 nm diameter MWNT that had a strong and uniform FWM signal in its pristine state. The total FWM signal decreased on each of two cycles of oxidation, approximately proportionally to the extent of the chemical modification. Fig. 6(b) provides complementary conductance information that is suggestive of the degree of damage done by each oxidation cycle. In this example, the first oxidation was performed in H<sub>2</sub>O, and it introduced enough disorder to reduce the conductance by one order of magnitude. The second oxidation was performed in H<sub>2</sub>SO<sub>4</sub> and extended until the conductance had decreased below 0.1 nS. Note that the oxidation of the first cycle was irreversible, so that no recovery in conductance is observed between the two cycles. In both cycles, a very mild oxidative potential allowed discrete drops in conductance to be resolved in time.<sup>37</sup>

Unlike previous ensemble FWM experiments,<sup>40</sup> the oxidative treatments used here do not remove carbon atoms from the CNT lattice, nor do they substantially reduce the number of free carriers. Instead,



the consequence of dilute oxidation is primarily to introduce electronic barriers along the CNT.<sup>38</sup> We conclude that a FWM intensity decrease occurs because these barriers severely limit coherent carrier oscillations, most dramatically in the case of SWNTs but also in MWNTs.

In addition to a uniform decrease in intensity, point-like, FWM-dark spots were also observed after dilute oxidation. Typically, only one or at most two dark sites accompanied the FWM decreases depicted in Fig. 6(a). However, subsequent cycles of oxidation drove the FWM signal fully to zero, and in that case the decrease became highly nonuniform and concentrated at particular positions along the MWNT length. Once a FWM-dark spot was observed, subsequent oxidation cycles seemed to concentrate the intensity decrease in the immediate region. These observations are consistent with our model of progressive oxidation, in which covalent modifications accumulate around initial nucleation sites because of their increased strain and a drive towards aromaticity.<sup>41</sup> Ultimately these insulating regions grow to the extent that they can be directly imaged by electron microscopy.<sup>42</sup> While the observed FWM-dark spots are clearly associated with sites where the oxidation initially nucleates, we have not quantitatively determined the FWM sensitivity limits, i.e. the minimum defect cluster size that was necessary to produce observable decreases in FWM intensity.

Additional experiments were performed in which portions of a CNT were exposed to the oxidizing electrolyte while the rest of the device remained protected. Oxidation was spatially limited by covering entire devices in an electron beam resist (polymethyl methacrylate, PMMA) and then using an electron beam to expose and develop small rectangular windows. In this manner, oxidation could be confined to a  $\sim 1\ \mu\text{m}$  length of CNT, in order to investigate differential FWM intensities from the oxidized and protected regions. After oxidation, the PMMA was entirely removed so that the different CNT segments were measured in similar dielectric environments.

Figs. 6(c) and 6(d) provide pairs of SEM and FWM images of two MWNTs oxidized in this manner. The highlighted boxes indicate the position of the PMMA window during oxidation, and the arrows depict the polarization of the excitation. The FWM intensity of the protected segments is substantially unchanged by the PMMA processing, and it therefore provides a reference for the exposed, oxidized

segments. In Fig. 6(c), the FWM intensity of the oxidized segment is reduced by 53%, and exhibits the nonuniform intensity described above. Fig. 6(d) shows a segment that was oxidized for a greater length of time, driving the FWM intensity down by 88% from its initial value. In both cases, AFM topography indicated no diameter changes along the CNT that would correspond to the removal of carbon material. Thus, the FWM darkening is not due to gross structural damage, but rather the effects of surface chemistry upon each CNT's electronic states. The results establish that FWM microscopy can spatially resolve the location of chemical attachments to the CNT sidewall, even in the dilute limit where these attachments are invisible to both SEM and AFM.

Finally, preliminary results suggest that the FWM signal may also be sensitive to different oxidation chemistries. Dilute electrochemical oxidations performed in different electrolytes have resulted in different amounts of FWM signal loss. For example, oxidation in glycolic acid followed by water rinsing resulted in much greater loss of FWM intensity than oxidation in glycolic acid alone, without rinsing. Alternatively, oxidation in HCl resulted in irreversible FWM signal decreases that occurred more rapidly than during similar oxidations in H<sub>2</sub>O. Further work with FWM signals may prove able to discriminate among the different possible types of sidewall chemical modifications.

### C.3. Strong Substrate Interactions

To further investigate environmental effects, FWM intensities were compared for SWNTs grown by the same CVD technique but on two different types of quartz substrates. The results described thus far come from SWNTs grown on fused quartz, a glassy surface on which the SWNTs have no preferred orientation. For comparison, SWNTs were also grown on single crystal substrates, for which 90% of all SWNTs were aligned along the quartz [100] crystal axis. The SWNT community knows that such alignment is common. While originally attributed to crystalline edge planes,<sup>43</sup> ongoing research suggests that SWNTs align during growth to particular crystallographic directions, either due to van der Waals interactions<sup>8</sup> or piezoelectric effects.<sup>24</sup> While the exact mechanisms remain unresolved, a strong consensus agrees that SWNTs have unusually strong interactions with crystalline quartz substrates.

Figure 7 shows that SWNTs aligned by the crystalline surface exhibited an almost fully quenched FWM response. On fused quartz, most SWNTs identified by SEM imaging are FWM bright [Fig. 7(a)]. The opposite is true on the single crystal quartz, where SEM imaging confirms the presence of many SWNTs that have no measurable FWM signal [Fig. 7(b)]. The alignment phenomenon allows individual SWNTs to be reliably located among much higher density growth, where the absence of FWM intensity from large numbers of SWNTs is most striking [Fig. 7(c)].

The histograms in Figure 8(a) summarize the FWM intensity distributions for both substrates. To generate the histogram, a particular  $100\text{ }\mu\text{m}^2$  area of dense aligned SWNT growth on the crystal quartz was chosen and the SWNTs were counted with SEM and compared to a FWM image of the same area. Figure 8(a) shows that 88% of these aligned SWNTs on crystal quartz were completely FWM dark. Areas with even denser SWNT growth also appeared dark, but could not be included in the histogram because of the difficulty of accurately counting individual SWNTs. Overall, we estimate that at least 95% of the SWNTs aligned on single crystal quartz are completely FWM dark, whether or not they are in contact with metal electrodes. This proportion is dramatically larger than SWNTs on fused quartz, for which only 10-30% are dark, depending on the gating conditions. Of the electrode-contacted SWNTs that were electrically tested across different crystalline samples, only one s-SWNT device displayed a weak but detectible intensity, and three m-SWNT devices had bright FWM signals. However, Fig. 8(b) shows that the m-SWNTs on crystal substrate had 50 to 70% less intensity than typical for m-SWNTs on fused quartz. Every remaining connection was completely FWM dark, even under conditions of moderate electrostatic gating.

On single crystal substrates, an additional, small number of SWNTs grew misaligned from the majority. These exceptions are believed to grow via a kite mechanism, in which synthesis occurs in the gas phase and then subsequently the SWNT lands and adheres to the substrate.<sup>44</sup> These misaligned SWNTs were found to share the typical electrical and optical characteristics of SWNTs on fused quartz, despite being found on the crystalline substrate. For example, two misaligned SWNTs are visible in the FWM image of Fig. 7(c). The significance of these examples is to prove that FWM quenching is not

merely caused by adhesion of SWNTs to a crystalline substrate. We conclude that quenching is instead caused by the same strong, crystallographic interaction that controls the aligned growth. This interaction might directly affect the optical transition probabilities, or it might indirectly result in SWNTs being synthesized with fundamentally different properties altogether.

Distinguishing between these two possible quenching mechanisms is experimentally complex, but two measurements suggest that a direct interaction of FWM processes with the quartz is the correct one. In one experiment, SWNTs were removed from crystalline quartz substrates and placed on fused quartz using a thermal tape transfer method that is becoming common in the study of SWNT films and graphene.<sup>45-47</sup> After transfer, many FWM dark SWNT films brightened and became more typical, as illustrated by the third histogram in Fig. 8(a). While the exact same SWNT was not imaged on both substrates, the overall brightening suggests that aligned SWNTs are not fundamentally different from misaligned ones.

A second type of measurement exploited the infrequent occurrence of SWNT being bent during growth. The vast majority of aligned SWNTs grow straight, but occasionally a SWNT deviates during growth so that one portion is aligned with the crystal axis and another is not. The inset of Fig. 7(d) shows an example of this phenomenon, where a single SWNT was found bent by  $75^\circ$ . By rotating the excitation polarization, the two segments of this SWNT could be imaged independently under identical experimental conditions. As shown in Fig. 7(d), the segment aligned with the crystal axis was entirely FWM dark, while the misaligned segment had a dim but otherwise typical FWM intensity. In almost every case of SWNTs incorporating similar kinks or bends, brightening occurred along the misaligned segments, and only a few exceptions remained FWM dark.

Both types of measurement support the conclusion that FWM depends on not just the SWNT properties but also the properties of the supporting surface. Some researchers have proposed that substrate-induced strain accompanies SWNT alignment,<sup>48</sup> as inferred from shifts in Raman peaks. In our experiments, widespread shifts were absent for the aligned SWNTs and only position-dependent variations were observed. An alternate proposal is that substrate-induced doping occurs on crystalline

quartz,<sup>24</sup>. This seems a more likely cause of the FWM quenching, since we observe strong dependence of FWM intensity on doping in s-SWNTs (Section C.1). It is possible that the effects of substrate-induced doping offset the strain-induced shifts in the Raman spectrum from our aligned SWNTs. Correctly determining the mechanisms that quench SWNT FWM signals will require further investigation.

Independently, Myllyperkio *et al.* have investigated FWM signals in two freely suspended s-SWNTs grown over trenches in a Si<sub>3</sub>N<sub>4</sub> substrate.<sup>12</sup> They found a strong FWM signal in one case and a very low FWM intensity in the other. Therefore, not all FWM variation among s-SWNTs can be attributed to substrate interactions. Nevertheless, this previous work did note much higher FWM signals from the Si<sub>3</sub>N<sub>4</sub>-supported portion than from the freely suspended portion of one s-SWNT, indicating an important role for substrates as described here. Unfortunately, substantial differences in the experimental excitation energies and fluence make it impossible to draw further comparisons with this work and our own.

#### C.4. Contamination and Inhomogeneity

Finally, we note that different CNTs can exhibit inhomogeneous FWM intensities. Two types of inhomogeneity are of particular concern and are described briefly here.

The interaction of a CNT with connective metal electrodes results in a number of electronic effects that can include contact resistance, Schottky barrier formation, and local carrier depletion or accumulation. Each of these interfacial effects is sensitive to the metal composition and the CNT bandstructure.<sup>49</sup> FWM intensity variations are very frequently observed within 300 nm of each CNT-metal interface and are presumably caused by the same interactions. Figs. 9(a) and 9(b) show examples of interfacial brightening or dimming that cause the FWM intensity to vary along a CNT. An analysis of these interfacial regions might be productively interpreted in terms of band bending and free carrier concentrations, in order to inform the study of depletion lengths in quasi-one dimensional systems.<sup>50</sup> In this report, however, these interface regions have been entirely excluded from the analysis. Saturated FWM intensities from Ti electrodes have already required selective image processing, so that further exclusion of 300 nm to either side of each electrode was straightforward to implement. Cr, Pd, and Ti

contacts all exhibited contact effects, and so all were excluded identically. Brightening was never observed at free CNT ends. Darkening, on the other hand, may have occurred, but it was impossible to distinguish from the CNT end itself given the limited spatial resolution of FWM imaging.

A second type of inhomogeneity was bright or dark FWM intensities at particular locations along the length of a CNT. While all FWM intensities fluctuate by at least 10% along CNT lengths, rare positions exhibited variations of 50% or more. Fig. 9(c) provides an example FWM image of one of these inhomogeneous sites. In some cases, FWM intensity variations along a single CNT could be attributed to kinks or contaminant particles resolved by AFM imaging. In other cases, no particular cause was evident, and the FWM inhomogeneities had no correlation with either topography or Raman D-band intensity. On the other hand, Raman G-band position and intensity does vary along the length of SWNTs, indicating the presence of charge density variations. We suspect that localized charging might cause both large and small amplitude FWM inhomogeneities. Charge traps in the underlying substrate are a ubiquitous source of density fluctuations, and they could certainly cause the smaller amplitude FWM variations seen along all samples. From an analysis of 30 CNTs with lengths up to 10  $\mu\text{m}$ , we estimate the larger amplitude inhomogeneities to have a mean separation of 3  $\mu\text{m}$ , which is consistent with earlier measurements of the mean defect density in SWNTs grown under similar CVD conditions.<sup>51</sup> Precisely correlating point defects with FWM intensity might be possible using near-field or tip-enhanced Raman,<sup>52, 53</sup> but performing such analysis is technically challenging. For this report, CNTs with spatially localized bright or dim segments were instead simply excluded from the analysis above, so that anomalous segments would not compromise reliable comparisons.

#### **D. Sensitivity to Excitation Wavelength**

The previous sections have focused on FWM variability caused by the type of CNT and its chemical environment. Here, we conclude with a section on the FWM optical technique itself, with particular attention to optical effects arising from either the experimental setup or the intrinsic optical CNT

properties. For instance, the polarization dependence noted in Section IIIB is a straightforward optical effect that has been demonstrated in previous work.<sup>11</sup> Here, new results focus on the role of excitation energy and details of the FWM emission spectra.

In photoluminescence, the spectra of CNTs can be mapped as a function of excitation energy to produce clear signatures of distinct morphologies.<sup>21</sup> Similar maps in FWM are far more difficult to accomplish, since the emission depends upon optical transitions at different frequencies  $\omega_p$  and  $\omega_s$ . Varying the two excitation sources independently can also change the combination frequency  $\omega_p \pm \omega_s$  and, in turn, affect the potential contribution of vibrational modes to FWM. Separating these effects, generating a full map of the excitation energy dependence, and distinguishing the role of phonons requires two, independently tunable sources so that  $\omega_p$  and  $\omega_s$  may be varied at fixed  $\omega_p - \omega_s$ . Instead of accomplishing this full mapping, we have instead conducted preliminary investigations using a single tunable source. In the following, we describe FWM signals measured using two different pairs of excitation pulses, each spaced to keep  $\omega_p - \omega_s$  fixed.

SWNTs have sharp optical resonances with large oscillator strengths,<sup>21, 30</sup> and to gauge their role in FWM we measured emission using two pairs of 200-fs excitation pulses. A lower energy pair ( $\lambda_p = 820$  nm,  $\lambda_s = 943$  nm; with  $\lambda_{as} = 725$  nm) and a higher energy pair ( $\lambda_p = 725$  nm,  $\lambda_s = 820$  nm; with  $\lambda_{as} = 650$  nm) were both tuned to have the same difference frequency, in order to gauge the emission's dependence on  $\omega_p$  or  $\omega_s$ , independent of the role of  $\omega_p - \omega_s$ . Within this limited test, the large majority of SWNTs exhibited only modest changes in FWM intensity, but approximately 20% (5 out of 22) exhibited very strong variations in FWM intensity.

Figure 10 highlights two extreme examples depicting FWM sensitivity to the excitation frequencies. In Fig. 10(a), the FWM intensity of a s-SWNT was very dim at  $\lambda_p = 820$  nm and  $\lambda_{as} = 725$  nm, but bright when excited by  $\lambda_p = 725$  nm and  $\lambda_{as} = 650$  nm. In Fig. 10(b), a larger diameter SWNT exhibited a similar degree of contrast change but under exactly the opposite conditions, with bright FWM signal at

the longer wavelengths. Simultaneously, a m-SWNT remained visible in the upper right portion of Fig. 10(b) but showed only a modest 25% change in contrast, which is more typical of SWNTs.

We can interpret the strong FWM variations in terms of the single-photon absorption cross sections at  $\omega_p$ . The s-SWNT of Fig. 10(a) had an AFM diameter  $D = 1.0 \pm 0.3$  nm, and an  $E_{22}$  close to 1.7eV that is nearly resonant with  $\lambda_p = 725$  nm, consistent with a (9,5) SWNT.<sup>3, 54</sup> The s-SWNT of Fig. 10(b), on the other hand, had an AFM diameter  $D = 2.4 \pm 0.5$  nm, a resonant Raman spectrum consistent with a large diameter, chiral SWNT, and an  $E_{22}$  that is more red-shifted and thus closer in pre-resonance with the  $\lambda_p = 820$  nm than with  $\lambda_p = 725$  nm. In both cases, exciting the SWNT near its optical transition resonance resulted in significantly higher FWM intensities from s-SWNTs that were otherwise dark. The fact that both SWNTs had a dark state implicates the role of extrinsic doping, and it is consistent with electrical measurements: both s-SWNTs were nonconductive at  $V_{bg} = 0$ , indicating  $E_F$  levels within the band gap. In fact, all of the SWNTs that showed strong excitation dependence were FWM dark in one of the pump configurations, and according to the discussion in Section B.1 this identifies them as undoped s-SWNTs. Thus, the conclusion that undoped s-SWNTs are generally dark must be amended for the special case when the excitation frequency  $\omega_p$  (and/or  $\omega_s$ ) is tuned to a SWNT optical resonance. The strong FWM signal observed in this condition may result from nonequilibrium carrier populations driven by enhanced, band-edge absorption.

Otherwise, approximately 80% of SWNTs behaved like the m-SWNT in Fig. 10(b), appearing similarly bright under both excitation conditions. The lack of any substantial dependence on excitation might simply indicate a mismatch of the SWNT one-photon resonances with  $\omega_p$  or  $\omega_s$ . Regardless of this possibility, though, the non-zero FWM signal under both excitation schemes indicates that these SWNTs must either be doped s-SWNTs or else m-SWNTs. In these cases, thermalized carrier populations already allow the FWM process depicted in Fig. 1(b), and perhaps the precise values of  $\omega_p$  and  $\omega_s$  only have secondary effects on the overall FWM yield. If correct, this interpretation predicts that only undoped s-



SWNTs will exhibit the dramatic FWM variations shown in Fig. 10, but this prediction has not been experimentally tested.

#### IV. CONCLUSION

In summary, we have examined the factors that influence the intensity of coherent FWM in individual CNTs using dual-color femtosecond laser excitation. Some of these factors included intrinsic properties of the CNT, such as diameter and electronic bandstructure. Among SWNTs, the FWM signal intensity was highest for m-SWNTs, smaller for doped s-SWNTs, and below detection-level for undoped, intrinsic s-SWNTs, making FWM a possible tool for wafer-scale optical discrimination of different types of SWNTs. Within each category, the intensity grew approximately quadratically with diameter. Both types of variation agree with an electronically-mediated FWM mechanism that is sensitive to free carrier concentration.

In addition to intrinsic variability, a number of extrinsic factors also affected FWM intensity, primarily through the dependence of CNT carrier concentration on environmental factors. By following individual SWNTs through a range of electrostatic doping, for example, a convincing one-to-one correspondence was proven between high conductivity and high FWM intensity. Similar results were demonstrated using noncovalent chemical doping and covalent chemical damage. In the latter case, average FWM intensity decreased proportionately to defect density, and intensity variations of up to 88% were observed at sites of electrochemically-introduced damage. The imaging of these inhomogeneous sites demonstrates that FWM might be applicable to defect imaging, at least within diffraction limits. The effect of substrate interactions also proved to be very important. Under optimum imaging conditions, 90% of SWNTs on fused quartz but only about 10% of SWNTs on crystal quartz were visible in FWM. Transferring SWNTs from one substrate to the other confirmed that the strong surface interactions of the crystal quartz substrate quenched the FWM signal.

The results presented in this work show that mapping individual CNTs with electronic FWM contrast provides useful information about the type of CNT and the interactions with its environment. Importantly,

this contrast can be obtained in a spatially resolved fashion, identifying spatial variations of the nonlinear response along the nanotube. The sensitivity of the FWM process to electrostatic gating and doping is particularly promising, as such relevant changes can be measured directly on the nanotubes that are incorporated into circuits. At relatively fast imaging speeds of  $\sim 10$  ms per pixel, such contrast may be beneficial for dynamically recording electronic or chemical changes in CNT systems. We therefore expect that, besides the vibrational CARS contrast, electronic FWM microscopy is a useful addition to the arsenal of CNT optical analysis techniques.

### ACKNOWLEDGEMENTS

This work was wholly supported by the NSF under grants DMR-0801271, DMR-1104629 and CHE-0802913.

### FIGURE CAPTIONS

**FIG. 1.** (color online) (a) and (b) Schematic of the experimental measurement technique. CNT devices are fabricated on quartz wafers and excited with a three-photon, two color scheme as shown. Emission is measured in the epi configuration. (c) Typical FWM image, with corresponding SEM image (inset), of a single SWNT connected to two Ti electrodes. The large FWM signal from the Ti enables rapid sample positioning and reliable focusing on the otherwise transparent surface. (d) FWM intensity profile between the electrodes, indicating the relative SWNT signal above the background dark count rate of the detector. The apparent width of the SWNT emission is diffraction limited.

**FIG. 2.** (color online) (a) Emission intensity from a MWNT as a function of delay between the pump and Stokes excitation pulses. At  $\Delta t = 0$ , the total signal combines all coherent processes. For  $\Delta t > 200$  fs, the

coherent FWM component has vanished but longer-lived processes like two-photon luminescence (TPEL) remain. (b) Emission spectrum for excitation by the pump beam (red), Stokes beam (black), and both beams (blue) at  $\Delta t = 0$ . Two-color excitation produces a narrow, coherent FWM peak at the anti-Stokes frequency and a small but spectrally broad TPEL signal. Repeating the measurement with an offset  $\Delta t = 1$  ps eliminates the FWM peak and shows that the TPEL component has decayed by only 50% (shown in inset).

**FIG. 3.** Spectrally-resolved emission from three different CNTs, each showing a FWM peak at  $\omega_{as}$  and a broad TPEL background. Similar measurements are necessary to estimate the fraction of emission at  $\omega_{as}$  that is due to FWM. Note that unlike the FWM, the TPEL component is not particularly sensitive to CNT structure.

**FIG. 4.** (color online) (a) SEM of multiple SWNTs in a single field of view. Characterization described in the text determines the type and diameter of each SWNT. Two parallel m-SWNTs are denoted by an asterisk, and a s-SWNT connecting three electrodes is denoted with a dagger. (b) Individual SWNTs exhibit widely varying FWM intensities, with some SWNTs remaining dark even when the excitation polarization (white arrow) is aligned parallel to them. (c) Analysis of multiple devices indicates that m-SWNTs are uniformly bright, while s-SWNTs fall into two categories, one of which is entirely dark.

**FIG. 5.** (color online) (a) Variation of FWM intensity (red) and conductance  $G$  (dashed black) in an electrostatically gated s-SWNT. Both go to zero at positive gate values that deplete the s-SWNT of carriers. (b) A simple energy diagram depicts the possibility of strong FWM signals when  $E_F$  is doped below the valence band edge by the amount  $\hbar(\omega_p - \omega_s)$ . (c) In a m-SWNT, both FWM intensity and  $G$  are susceptible to modulation on the order of 50%, but neither signal can be gated to zero. (d) Energy

diagram in accord with the experimental measurement. In (b) and (d), labels correspond to conventional optical SWNT transitions as described in the text.

**FIG. 6.** (color online) (a) Decrease of FWM intensity from a MWNT following two 60-second cycles of dilute electrochemical oxidation. (b) The degree of oxidation on individual MWNTs is controlled by monitoring the MWNT conductance, which is far more sensitive to oxidation than the FWM signal. (c) SEM and FWM images for a similar MWNT device that had been mostly protected by a PMMA coating. Electrochemical oxidation of the MWNT was restricted to a small exposure window developed in the PMMA, indicated by the dashed line. After oxidation as in (a) and removal of the PMMA, SEM imaging could not resolve the chemical damage. The FWM intensity decreased inhomogeneously, to an average value 53% smaller than for the protected MWNT sections. (d) A similar experiment with a harsher oxidation resulted in an 88% FWM intensity decrease in an exposed segment. Excitation polarization is depicted with white arrows.

**FIG. 7.** (color online) (a) Typical SEM (left) and FWM (right) images for SWNTs grown dilutely on fused quartz. (b) Comparison images for SWNTs on ST-cut, single crystal quartz, grown at similar density. On the single crystal substrate, none of the SWNTs appear in the FWM image. (c) On single crystal quartz, high density growth is required to observe any SWNTs in the FWM image, and the majority of these are misaligned from the preferred growth direction. The result suggests that surface interactions with the crystal step edges quench the FWM signal. Excitation polarization is depicted in each image with white arrows, and electrode intensity varies from sample to sample due to electrode metal composition and laser exposure history. (d) FWM intensity for two portions of a single, bent SWNT, measured independently by aligning the excitation polarization with one segment or the other. The SWNT is dark when parallel to the [100] step edge, but FWM-bright when misaligned by 90°. The inset shows an SEM image of the SWNT.

**FIG. 8.** (color online) (a) FWM intensity distribution of CNTs on three different substrates. Compared to the typical distribution observed on fused quartz, SWNTs on ST-quartz are predominantly dark. The dark fraction drops to 65% when the same SWNTs are transferred from the ST-quartz substrate to a fused or amorphous quartz substrate. (b) Even among the few m-SWNTs that remain bright on ST-quartz, a direct comparison of FWM intensities to m-SWNTs on fused quartz shows a substantially lower signal. FWM intensity profiles from two different m-SWNTs on each substrate are shown.

**FIG. 9.** (color online) (a) The most common type of FWM intensity inhomogeneity is an enhancement surrounding the SWNT-metal electrode interface. The enhanced regions appear to extend 300 nm away from the metal. (b) Diminished FWM intensity is observed more rarely, perhaps due to exceptionally poor electrical contacts. (c) SWNTs with contaminant particles can likewise exhibit inhomogeneous FWM intensities, causing either bright or dark portions.

**FIG. 10.** (color online) (a) FWM signal from a s-SWNT shows two different intensities depending on the excitation wavelengths. A very weak signal is observed using 820 and 943 nm pulses (red curve and upper image), but strong enhancement is observed using 725 and 820 nm pulses (blue curve, lower image). (b) A different s-SWNT shows the opposite contrast behavior, despite being imaged with identical imaging conditions. A m-SWNT in the upper right corner of the same image remains similarly bright under both excitations. Excitation polarization is depicted by the white arrow.

## REFERENCES

\*Corresponding Author: collinsp@uci.edu

- <sup>1</sup> P. Avouris, M. Freitag, and V. Perebeinos, in *Carbon Nanotubes*, edited by A. Jorio, G. Dresselhaus and M. S. Dresselhaus (Springer-Verlag, Berlin, 2008), Vol. 111, p. 423.
- <sup>2</sup> J. Lefebvre, S. Maruyama, and P. Finnie, in *Carbon Nanotubes*, edited by A. Jorio, G. Dresselhaus and M. S. Dresselhaus (Springer-Verlag, Berlin, 2008), Vol. 111, p. 287.
- <sup>3</sup> R. Saito, C. Fantini, and J. Jiang, in *Carbon Nanotubes*, edited by A. Jorio, G. Dresselhaus and M. S. Dresselhaus (Springer-Verlag, Berlin, 2008), Vol. 111, p. 287.
- <sup>4</sup> R. W. Havener, A. W. Tsen, H. C. Choi, and J. Park, *NPG Asia Mater.* **3**, 91 (2011).
- <sup>5</sup> X. C. Liu, et al., *Appl. Phys. Lett.* **74**, 164 (1999).
- <sup>6</sup> D. Shimamoto, T. Sakurai, M. Itoh, Y. A. Kim, T. Hayashi, M. Endo, and M. Terrones, *Appl. Phys. Lett.* **92**, 081902 (2008).
- <sup>7</sup> F. Wang, A. G. Rozhin, V. Scardaci, Z. Sun, F. Hennrich, I. H. White, W. I. Milne, and A. C. Ferrari, *Nature Nanotechnol.* **3**, 738 (2008).
- <sup>8</sup> A. G. Rozhin, Y. Sakakibara, S. Namiki, M. Tokumoto, H. Kataura, and Y. Achiba, *Appl. Phys. Lett.* **88**, 051118 (2006).
- <sup>9</sup> M. W. Graham, Y. Z. Ma, and G. R. Fleming, *Nano Lett.* **8**, 3936 (2008).
- <sup>10</sup> Y. J. Lee, S. H. Parekh, J. A. Fagan, and M. T. Cicerone, *Phys. Rev. B* **82**, 165432 (2010).
- <sup>11</sup> H. Kim, T. Sheps, P. G. Collins, and E. O. Potma, *Nano Lett.* **9**, 2991 (2009).
- <sup>12</sup> P. Myllyperkio, et al., *ACS Nano* **4**, 6780 (2010).
- <sup>13</sup> L. Tong, Y. Liu, B. D. Dolash, Y. Jung, M. N. Slipchenko, D. E. Bergstrom, and J. X. Cheng, *Nature Nanotechnol.* **7**, 56 (2011).
- <sup>14</sup> K. Furusawa, N. Hayazawa, F. C. Catalan, T. Okamoto, and S. Kawata, *J. Raman Spectrosc.* **43**, 656 (2011).
- <sup>15</sup> E. Joselevich, H. Dai, J. Liu, K. Hata, and A. H. Windle, in *Carbon Nanotubes*, edited by A. Jorio, G. Dresselhaus and M. S. Dresselhaus (Springer-Verlag, Berlin, 2008), Vol. 111, p. 101.
- <sup>16</sup> G. D. Nessim, *Nanoscale* **2**, 1306 (2010).
- <sup>17</sup> L. An, J. M. Owens, L. E. McNeil, and J. Liu, *J. Am. Chem. Soc.* **124**, 13688 (2002).
- <sup>18</sup> A. Müller, S. K. Das, P. Kogerler, H. Bogge, M. Schmidtman, A. X. Trautwein, V. Schunemann, E. Krickemeyer, and W. Preetz, *Angew. Chem.-Int. Edit.* **39**, 3414 (2000).
- <sup>19</sup> S. M. Huang, B. Maynor, X. Y. Cai, and J. Liu, *Adv. Mater.* **15**, 1651 (2003).
- <sup>20</sup> Y. Wang, C. Y. Lin, A. Nikolaenko, V. Raghunathan, and E. O. Potma, *Adv. Opt. Photon.* **3**, 1 (2011).

- <sup>21</sup> S. M. Bachilo, M. S. Strano, C. Kittrell, R. H. Hauge, R. E. Smalley, and R. B. Weisman, *Science* **298**, 2361 (2002).
- <sup>22</sup> J. Lefebvre, Y. Homma, and P. Finnie, *Phys. Rev. Lett.* **90**, 217401 (2003).
- <sup>23</sup> J. X. Cheng and X. S. Xie, *J. Phys. Chem. B* **108**, 827 (2004).
- <sup>24</sup> J.-X. Cheng, A. Volkmer, and X. S. Xie, *J. Opt. Soc. Am. B* **19**, 1363 (2002).
- <sup>25</sup> R. B. Weisman and S. M. Bachilo, *Nano Lett.* **3**, 1235 (2003).
- <sup>26</sup> R. Martel, T. Schmidt, H. R. Shea, T. Hertel, and P. Avouris, *Appl. Phys. Lett.* **73**, 2447 (1998).
- <sup>27</sup> S. J. Tans, A. R. M. Verschueren, and C. Dekker, *Nature* **393**, 49 (1998).
- <sup>28</sup> M. Kruger, M. R. Buitelaar, T. Nussbaumer, C. Schonenberger, and L. Forro, *Appl. Phys. Lett.* **78**, 1291 (2001).
- <sup>29</sup> S. Rosenblatt, Y. Yaish, J. Park, J. Gore, V. Sazonova, and P. L. McEuen, *Nano Lett.* **2**, 869 (2002).
- <sup>30</sup> M. J. O'Connell, et al., *Science* **297**, 593 (2002).
- <sup>31</sup> S. Ilani, L. A. K. Donev, M. Kindermann, and P. L. McEuen, *Nature Physics* **2**, 687 (2006).
- <sup>32</sup> R. Tu, L. Zhang, Y. Nishi, and H. J. Dai, *Nano Lett.* **7**, 1561 (2007).
- <sup>33</sup> H. Kataura, Y. Kumazawa, Y. Maniwa, I. Umezu, S. Suzuki, Y. Ohtsuka, and Y. Achiba, *Synth. Met. (Switzerland)* **103**, 2555 (1999).
- <sup>34</sup> Y. F. Lian, Y. Maeda, T. Wakahara, T. Akasaka, S. Kazaoui, N. Minami, N. Choi, and H. Tokumoto, *J. Phys. Chem. B* **107**, 12082 (2003).
- <sup>35</sup> M. Ouyang, J. L. Huang, C. L. Cheung, and C. M. Lieber, *Science* **292**, 702 (2001).
- <sup>36</sup> J. G. Coroneus, B. R. Goldsmith, J. A. Lamboy, A. A. Kane, P. G. Collins, and G. A. Weiss, *ChemPhysChem* **9**, 1053 (2008).
- <sup>37</sup> B. R. Goldsmith, J. G. Coroneus, V. R. Khalap, A. A. Kane, G. A. Weiss, and P. G. Collins, *Science* **315**, 77 (2007).
- <sup>38</sup> S. R. Hunt, D. Wan, V. R. Khalap, B. L. Corso, and P. G. Collins, *Nano Lett.* **11**, 1055 (2011).
- <sup>39</sup> Y. Kanai, V. R. Khalap, P. G. Collins, and J. C. Grossman, *Phys. Rev. Lett.* **104**, 066401 (2010).
- <sup>40</sup> K. C. Jena, P. B. Bisht, M. M. Shaijumon, and S. Ramaprabhu, *Optics Communications* **273**, 153 (2007).
- <sup>41</sup> M. K. Ashraf, N. A. Bruque, R. R. Pandey, P. G. Collins, and R. K. Lake, *Phys. Rev. B* **79**, 115428 (2009).
- <sup>42</sup> Y. Zhang and Y. Wang, *Journal of Physical Chemistry Letters* **2**, 885 (2011).
- <sup>43</sup> A. Ismach, L. Segev, E. Wachtel, and E. Joselevich, *Angewandte Chemie-International Edition* **43**, 6140 (2004).
- <sup>44</sup> S. M. Huang, M. Woodson, R. Smalley, and J. Liu, *Nano Lett.* **4**, 1025 (2004).
- <sup>45</sup> K. Ryu, et al., *Nano Lett.* **9**, 189 (2009).

- <sup>46</sup> L. Ding, A. Tselev, J. Wang, D. Yuan, H. Chu, T. P. McNicholas, Y. Li, and J. Liu, *Nano Lett.* **9**, 800 (2009).
- <sup>47</sup> N. Patil, A. Lin, E. R. Myers, K. Ryu, A. Badmaev, C. W. Zhou, H. S. P. Wong, and S. Mitra, *Ieee Transactions on Nanotechnology* **8**, 498 (2009).
- <sup>48</sup> T. Ozel, D. Abdula, E. Hwang, and M. Shim, *ACS Nano* **3**, 2217 (2009).
- <sup>49</sup> S. Heinze, J. Tersoff, R. Martel, V. Derycke, J. Appenzeller, and P. Avouris, *Phys. Rev. Lett.* **89**, 106801 (2002).
- <sup>50</sup> F. Leonard and D. A. Stewart, *Nanotechnology* **17**, 4699 (2006).
- <sup>51</sup> Y. Fan, B. R. Goldsmith, and P. G. Collins, *Nat. Mat.* **4**, 906 (2005).
- <sup>52</sup> A. Hartschuh, E. J. Sanchez, X. S. Xie, and L. Novotny, *Phys. Rev. Lett.* **90**, 095503 (2003).
- <sup>53</sup> N. Anderson, A. Hartschuh, S. Cronin, and L. Novotny, *J. Am. Chem. Soc.* **127**, 2533 (2005).
- <sup>54</sup> A. Jorio, R. Saito, J. H. Hafner, C. M. Lieber, M. Hunter, T. McClure, G. Dresselhaus, and M. S. Dresselhaus, *Phys. Rev. Lett.* **86**, 1118 (2001).



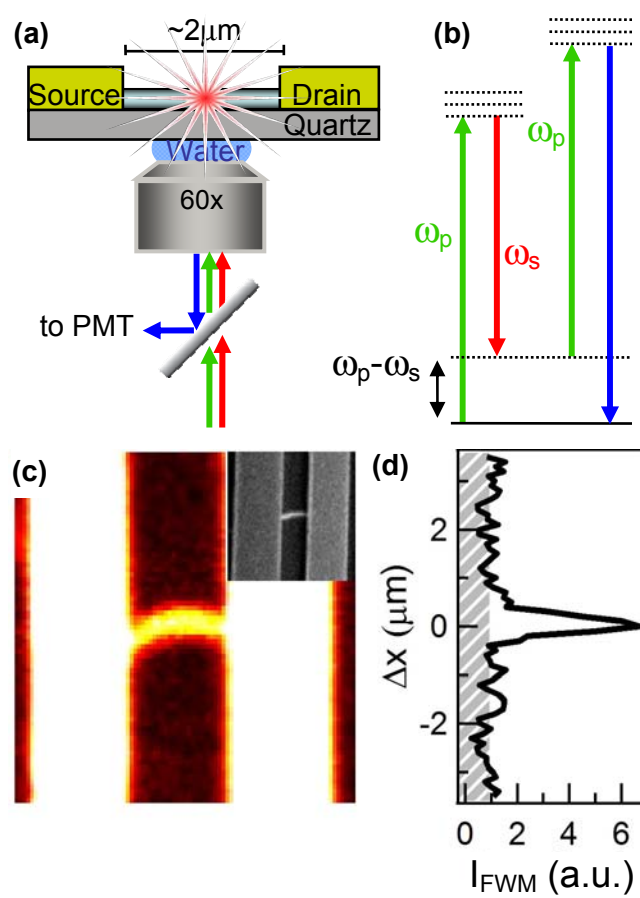


FIG. 1.

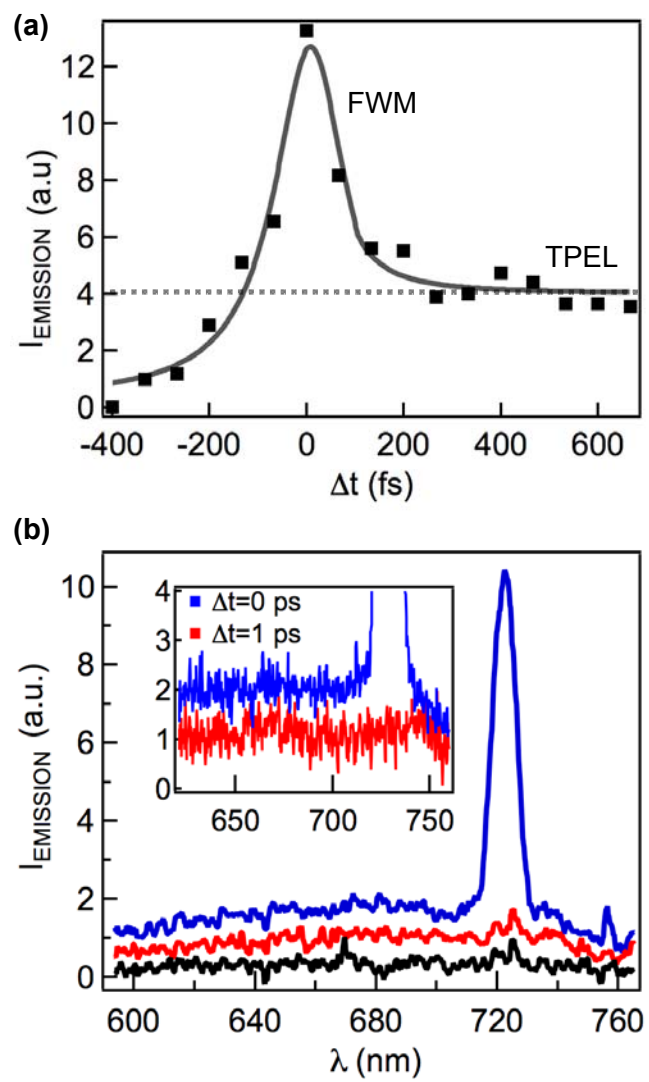
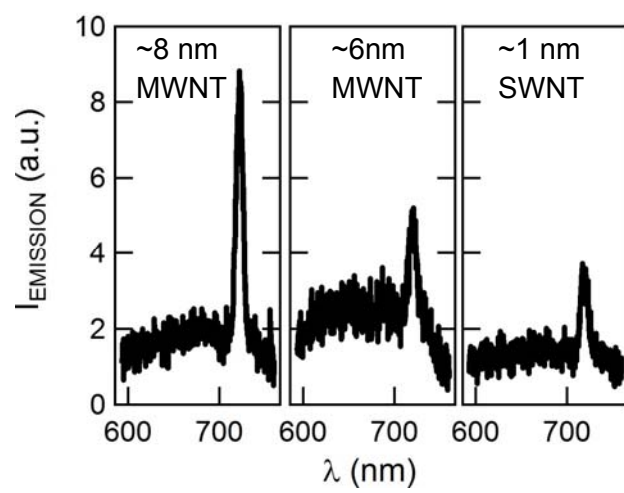


FIG. 2.



**FIG. 3.**

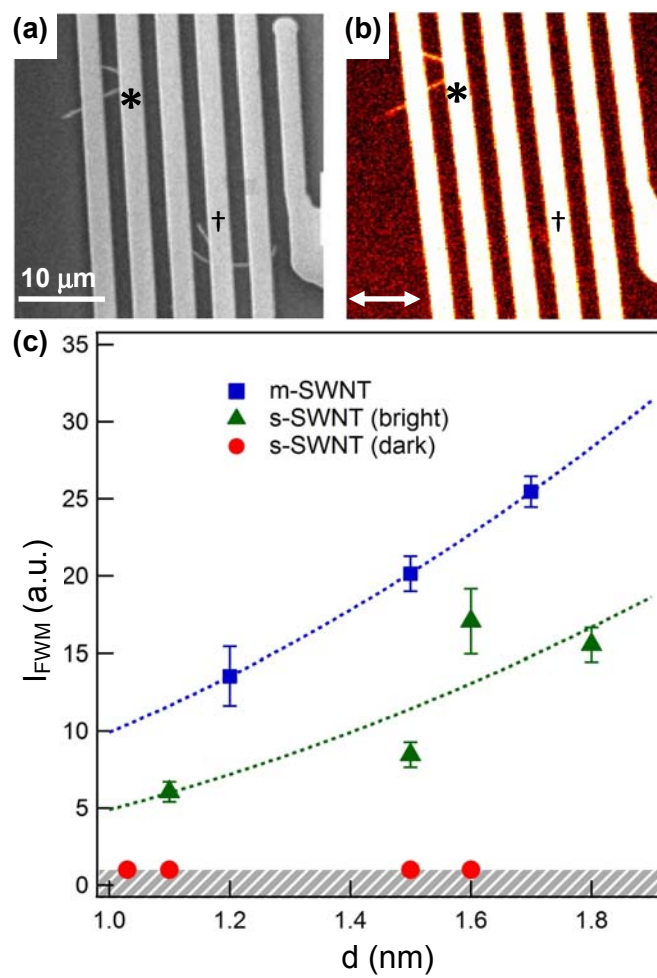


FIG. 4.

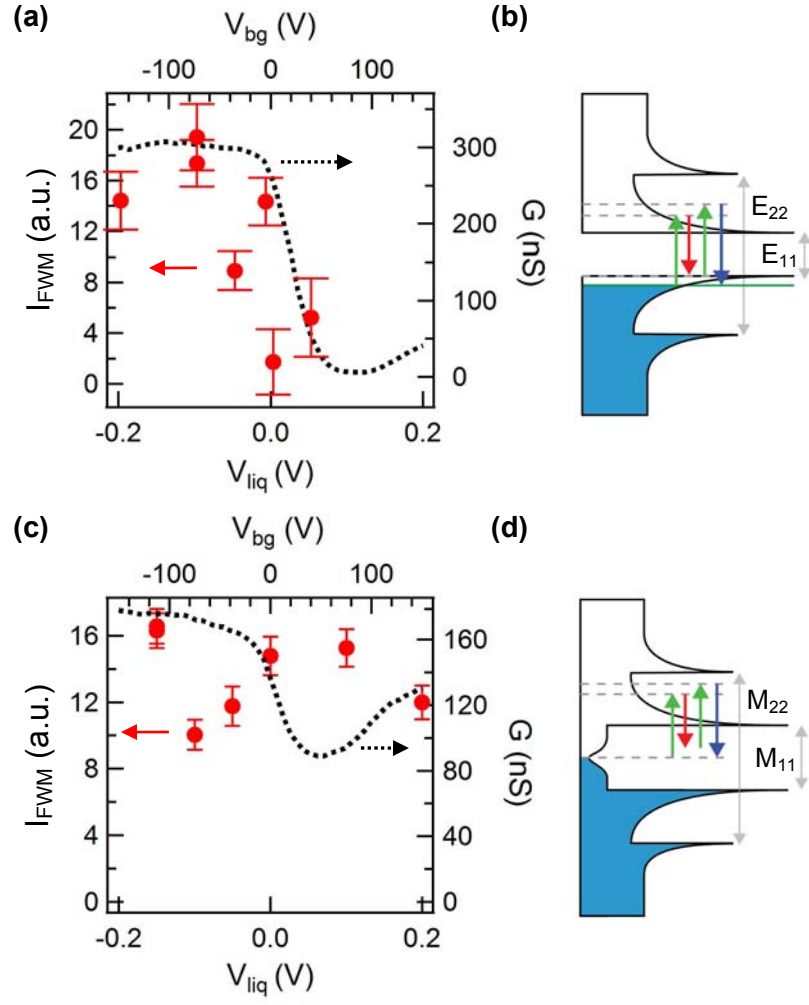


FIG. 5.

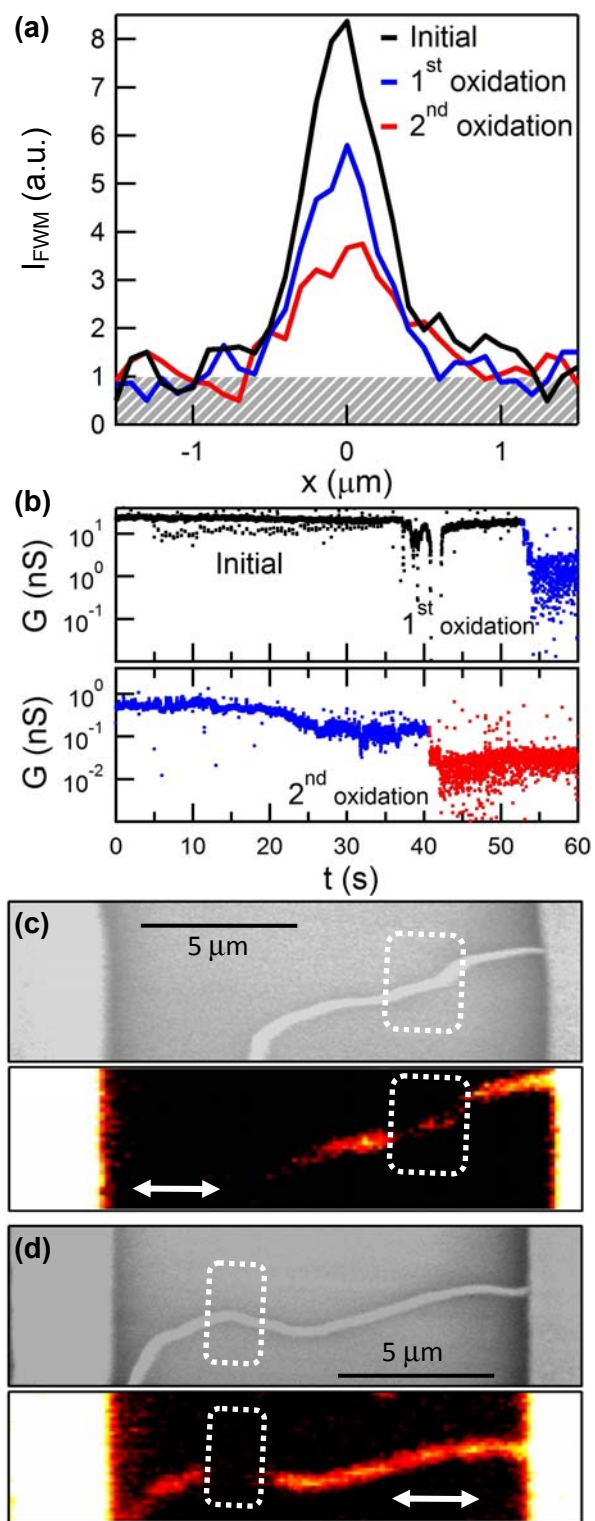


FIG. 6

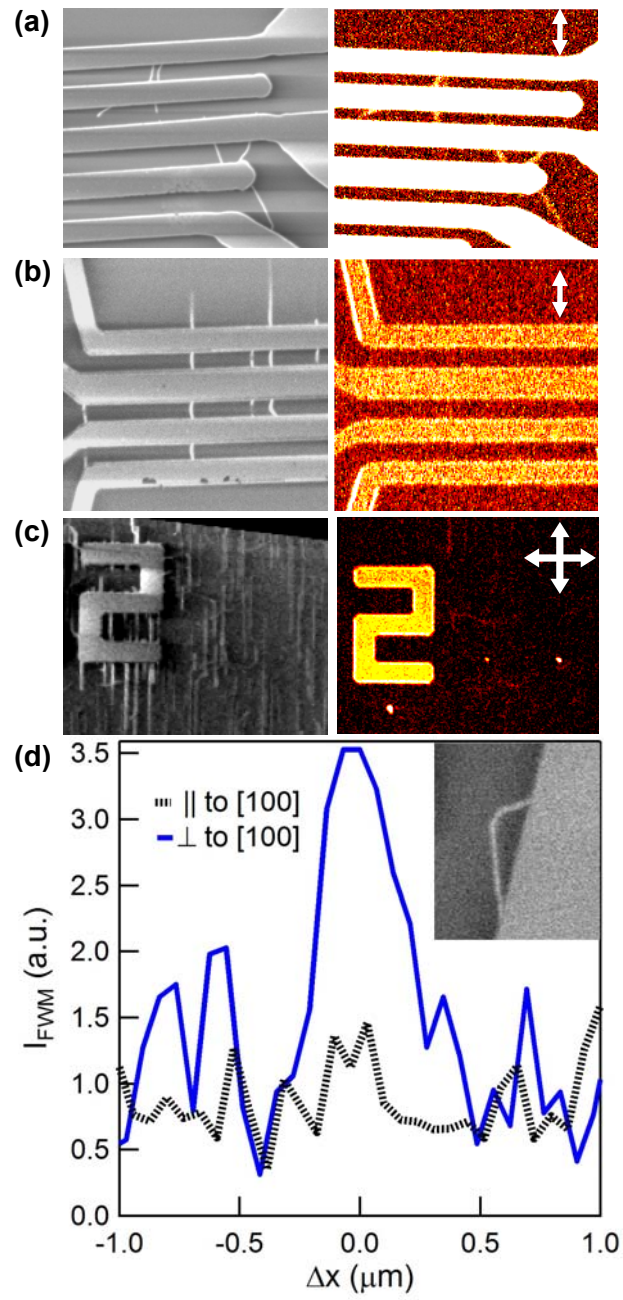


FIG. 7

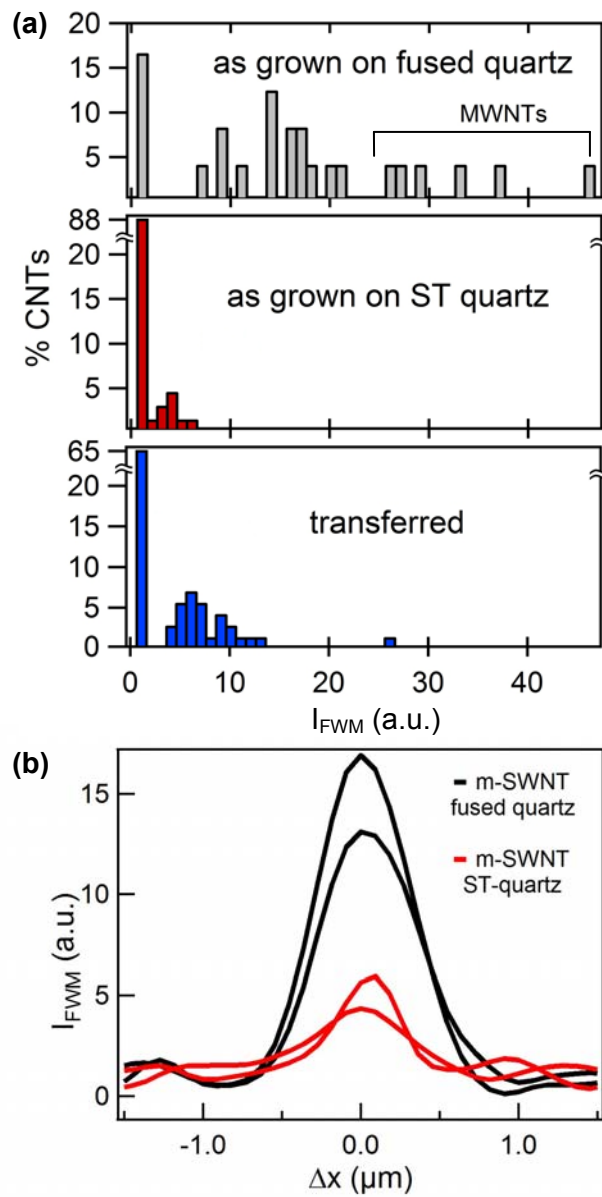
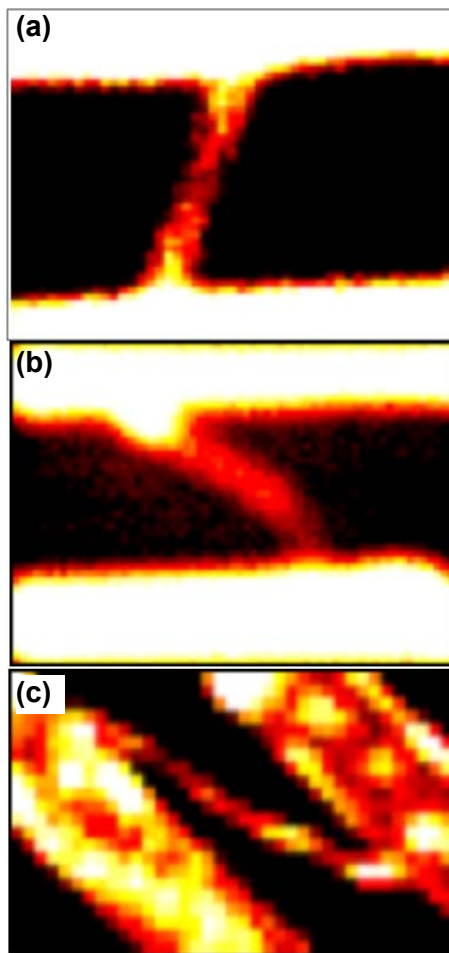


FIG. 8.





**FIG. 9.**

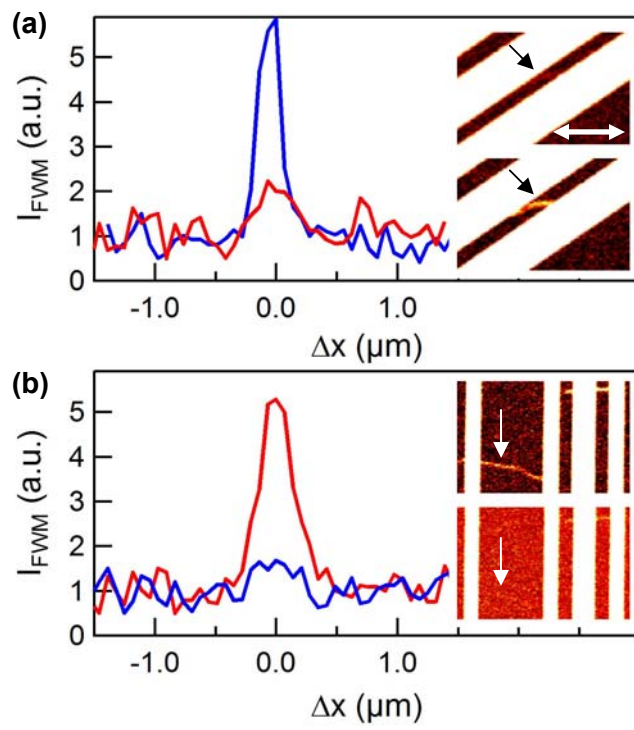


FIG. 10.